



HAL
open science

On the modelling of joint formation in dissolutive brazing processes

Michael Vynnycky, Jacques Lacaze

► **To cite this version:**

Michael Vynnycky, Jacques Lacaze. On the modelling of joint formation in dissolutive brazing processes. *Journal of Engineering Mathematics*, 2019, 116 (1), pp.73-99. 10.1007/s10665-019-10003-z . hal-02458184

HAL Id: hal-02458184

<https://hal.science/hal-02458184>

Submitted on 28 Jan 2020

HAL is a multi-disciplinary open access archive for the deposit and dissemination of scientific research documents, whether they are published or not. The documents may come from teaching and research institutions in France or abroad, or from public or private research centers.

L'archive ouverte pluridisciplinaire **HAL**, est destinée au dépôt et à la diffusion de documents scientifiques de niveau recherche, publiés ou non, émanant des établissements d'enseignement et de recherche français ou étrangers, des laboratoires publics ou privés.



Open Archive Toulouse Archive Ouverte (OATAO)

OATAO is an open access repository that collects the work of Toulouse researchers and makes it freely available over the web where possible

This is an author's version published in: <http://oatao.univ-toulouse.fr/25344>

Official URL: <https://doi.org/10.1007/s10665-019-10003-z>

To cite this version:

Vynnycky, Michael and Lacaze, Jacques  *On the modelling of joint formation in dissolutive brazing processes.* (2019) *Journal of Engineering Mathematics*, 116 (1). 73-99. ISSN 0022-0833

Any correspondence concerning this service should be sent to the repository administrator: tech-oatao@listes-diff.inp-toulouse.fr

On the modelling of joint formation in dissolutive brazing processes

M. Vynnycky  · J. Lacaze

Abstract In this paper, earlier dissolutive wetting models describing the dynamics of an axisymmetric alloy drop spreading on pure metal substrate are extended to describe reactive wetting and subsequent joint formation in brazing processes. A two-dimensional time-dependent problem is formulated, and the model equations are nondimensionalized, revealing the possibilities for asymptotic model reduction. Whilst the numerical solution of the time-dependent problem, which contains two moving contact lines and would not in general be amenable to lubrication theory, is relegated to future work, the steady-state problem is analyzed in detail. The analysis offers an arguably more transparent alternative to an earlier energy minimization approach for finding the location of the meniscus, which ultimately constitutes the joint. The results of the present model are found to compare favourably to those of earlier experimental and theoretical work.

Keywords Asymptotic analysis · Dissolution · Wetting

1 Introduction

In the controlled atmosphere brazing (CAB) process, separate parts are assembled by being submitted to a thermal cycle during which a cladding consisting of a low melting temperature alloy becomes liquid and forms the necessary joints by capillarity. After a time allocated for joint formation, the assembly is cooled so that the joints solidify. For manufacturing aluminium heat exchangers, the parts to be assembled are plates and fins made of an essentially binary Al–Mn alloy. Some of these parts are clad with an essentially binary Al–Si alloy that has a liquidus 40–50 K below the solidus of the Al–Mn alloy. Proper joint formation requires that enough liquid is made available to form the joints, but not too much as this may lead to unexpected deformations of the assemblies and other potential

M. Vynnycky (✉)

Division of Processes, Department of Materials Science and Engineering, Royal Institute of Technology, Brinellvägen 23, 100 44 Stockholm, Sweden
e-mail: michael.vynnycky@ul.ie

M. Vynnycky

Present Address: Department of Mathematics and Statistics, University of Limerick, Limerick V94 T9PX, Ireland

J. Lacaze

CIRIMAT, Université de Toulouse, 4 allée Emile Monso – CS44362, 31030 Toulouse Cedex 4, France

defects. Accordingly, the brazing cycles are designed with a maximum temperature close to the clad alloy liquidus, slightly lower to minimize deformations or slightly higher if more liquid is needed.

Since the very beginning of development of the CAB process, the materials and process parameters have been tested using an inverted tee-joint configuration, wherein a plate stands vertically on a horizontal plate [1–3]. A theoretical prediction of the brazed joint shape to be formed during manufacturing can be performed using a joint shape modelling advocated in [4]. Recent studies of some relatively simple brazed joint configurations [5], and more complex two-dimensional (2D) and three-dimensional (3D) geometries [6,7], have convincingly demonstrated that a minimization of potential energy of the molten metal free surface at the onset of cladding solidification may efficiently be utilized for joint topology predictions. A summary of these approaches is given in [8].

Nevertheless, the modelling of brazing should be amenable to an even more fundamental approach, such as that which has been applied to reactive wetting in metal–metal systems [9–13]. Thus, rather than appealing to energy minimization so as to find, for example, the final equilibrium meniscus shape, it should be possible to formulate time-dependent conservation equations that describe how the final state is reached. One reason this approach has not been adopted for brazing is that it has been proven difficult to obtain solutions for real parameters in solder systems [5,14]. Hence, one of the aims of this paper is to apply the concepts previously used for reactive wetting to the modelling of microscale phenomena in brazing. Moreover, this approach should serve to complement the energy minimization approach: for example, it is already a well-accepted concept in physics that the shape that a fluid meniscus adopts is the same as that required to minimize the energy of the system [15].

To fix ideas, we focus on the inverted tee-joint configuration considered in [5], as it is not only the simplest one to consider geometrically, but there are also experimental data to compare with. The structure of the paper is as follows. In Sect. 2, we motivate the modelling approach to be used. In Sect. 3, we formulate the problem mathematically, and in Sect. 4, we nondimensionalize the equations. The main body of the analysis is in Sect. 5, which considers the time-dependent equations from a qualitative perspective and the solution of the steady-state equations. Results are given in Sect. 6, and conclusions are drawn in Sect. 7. Finally, auxiliary results are given in four appendices.

2 Modelling considerations

Compared to the modelling of reactive spreading of an axisymmetric droplet of a molten metallic alloy on a metal substrate [9–13], the modelling of brazing is substantially more complex, since the clad, which will ultimately flow and cause the dissolution of the core, is initially solid. Moreover, once the heating of the core–clad assembly starts, solid-state diffusion of the silicon in the clad occurs; also, it may be the case that heating is not isothermal, with different parts of the clad and the core reaching a certain temperature at different times. In particular, this will mean that some parts of the clad will reach the solidus temperature sooner than others; thus, these parts would in principle be available for flow sooner than others. However, if there is no solid-state diffusion from the clad to the core and if the final holding temperature is lower than the liquidus temperature corresponding to the initial composition of Si in the clad, then not all of the clad will melt; on the other hand, if there is solid-state diffusion, then even this holding temperature might not be high enough to melt the clad, and an even higher temperature would be required to do so. Furthermore, once melting has begun, capillary forces can be expected to disrupt the initial planar configuration of the clad, leading to the formation of a moving meniscus, at which point coupled two-phase momentum, i.e. heat and solute transfers will be occurring. A more complete description of these stages can be found in [16].

Therefore, in order to avoid getting bogged down in these details, and to be able to focus on reactive spreading, we will simply assume that the clad is initially molten and at a uniform temperature that is greater than the liquidus temperature for the clad; furthermore, we will also assume that the core is at the same uniform temperature as the clad. In fact, these assumptions should not affect what will be the main body of the results in this paper, i.e. the determination at steady state of the joint shape and of the dissolved region.

3 Model formulation

3.1 Governing equations

Assume all of the clad, of composition c_0 , has reached the temperature T , where $T > T_{liq}(c_0)$ and occupies $0 \leq x \leq w_0, 0 \leq y \leq h_0$, as shown in Fig. 1, which depicts the right-hand half of an inverted tee joint. Here, T_{liq} denotes the liquidus curve in the Al–Si phase diagram and is a function of the Si concentration, c , as shown in Fig. 2a; however, in what follows, we approximate T_{liq} by

$$T_{liq} = T_m - mc, \quad (3.1)$$

where T_m denotes the melting temperature of pure aluminium and $-m$ is the slope of the liquidus curve, which is now assumed straight, as is shown in Fig. 2b. Thus, $T > T_{liq}(c_0)$ implies that the clad is assumed to be completely molten initially. Note also that we implicitly assume that the horizontal core and clad are initially in contact, so that the clad immediately proceeds to wet the core; clearly, in practice, this contact may be limited or sporadic along the length of the joint, leading to possible variations along the axis perpendicular to the x – y plane that we consider. Thereafter, the molten clad begins to move and at time t , it will occupy $0 \leq x \leq x_1(t), 0 \leq y \leq h(x, t)$, as shown in Fig. 3. At the same time, the core which occupies $x < 0$ and $y < 0$ will dissolve, with the limit of the

Fig. 1 Initial configuration for an inverted tee joint

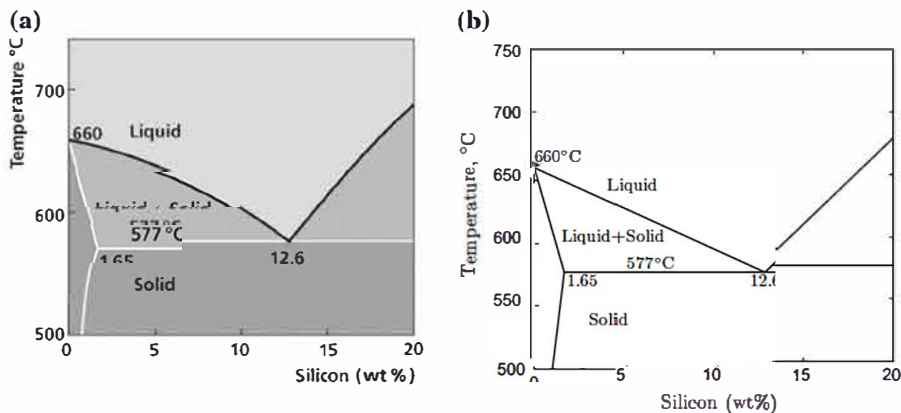
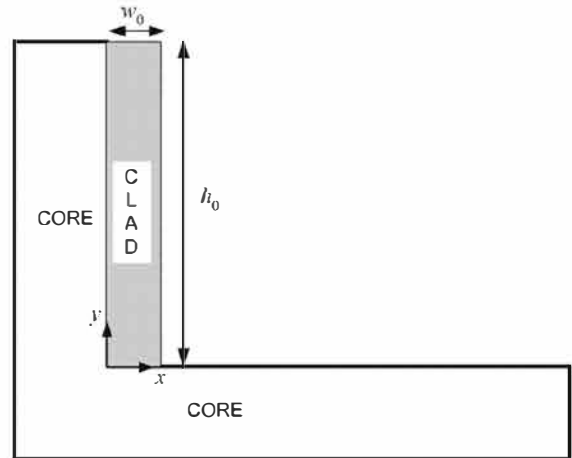
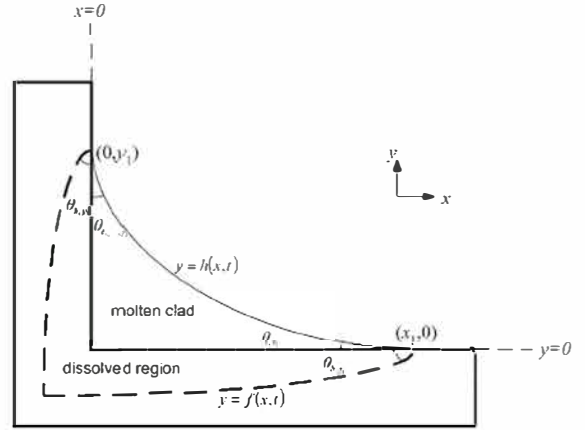


Fig. 2 a Actual Al–Si phase diagram; b Linearized Al–Si phase diagram

Fig. 3 Schematic of the molten clad and dissolved region during dissolution



dissolved region defined by $y = f(x, t)$. Also, we have the equation of continuity and the x - and y -components of the Navier–Stokes equation, for $f(x, t) \leq y \leq h(x, t)$,

$$\frac{\partial u}{\partial x} + \frac{\partial v}{\partial y} = 0, \quad (3.2)$$

$$\rho \left(\frac{\partial u}{\partial t} + u \frac{\partial u}{\partial x} + v \frac{\partial u}{\partial y} \right) = -\frac{\partial p}{\partial x} + \mu \left(\frac{\partial^2 u}{\partial x^2} + \frac{\partial^2 u}{\partial y^2} \right), \quad (3.3)$$

$$\rho \left(\frac{\partial v}{\partial t} + u \frac{\partial v}{\partial x} + v \frac{\partial v}{\partial y} \right) = -\frac{\partial p}{\partial y} + \mu \left(\frac{\partial^2 v}{\partial x^2} + \frac{\partial^2 v}{\partial y^2} \right) - \rho g, \quad (3.4)$$

where ρ and μ are, respectively, the density and viscosity of molten clad; these will be assumed to be constant. In addition, u and v are the velocity components in the x - and y -directions respectively, p is the pressure and g is the gravitational acceleration. Moreover, conservation of solute is given by

$$\frac{\partial c}{\partial t} + u \frac{\partial c}{\partial x} + v \frac{\partial c}{\partial y} = D \left(\frac{\partial^2 c}{\partial x^2} + \frac{\partial^2 c}{\partial y^2} \right), \quad f(x, t) \leq y \leq h(x, t), \quad (3.5)$$

where c is the solute concentration and D is the diffusion coefficient for Si. Also, by conservation of mass for the clad, we must have

$$\int_0^{x_1(t)} h(x, t) dx = w_0 h_0. \quad (3.6)$$

3.2 Boundary conditions

At $y = h(x, t)$, we have zero tangential stress, given by

$$2\mu \left(\frac{\partial v}{\partial y} - \frac{\partial u}{\partial x} \right) h_x + \mu \left(\frac{\partial u}{\partial y} + \frac{\partial v}{\partial x} \right) \left\{ 1 - h_x^2 \right\} = 0, \quad (3.7)$$

and a normal stress condition, given by

$$p_a - p + \frac{2\mu}{1 + h_x^2} \left\{ \frac{\partial u}{\partial x} h_x^2 + \frac{\partial v}{\partial y} - \left(\frac{\partial u}{\partial y} + \frac{\partial v}{\partial x} \right) h_x \right\} = \sigma_{fs} \mathcal{K}, \quad (3.8)$$

where σ_{fs} denotes the interfacial tension between the molten clad and the surroundings, p_a is the pressure of the surroundings and \mathcal{K} is the curvature of the meniscus, given by

$$\mathcal{K} = \frac{h_{xx}}{1 + h_x^2}^{3/2}. \quad (3.9)$$

In addition to (3.7) and (3.8), which are called dynamic conditions, there is a kinematic condition for the motion of the meniscus, given by

$$v = h_t + u h_x. \quad (3.10)$$

Also, there is no normal flux of solute at the meniscus, and hence

$$\mathbf{n}_h \cdot \nabla c = 0, \quad (3.11)$$

where \mathbf{n}_h is the unit normal vector to $y = h(x, t)$, and is given by

$$\mathbf{n}_h = \frac{1}{\sqrt{1 + h_x^2}} (-h_x, 1). \quad (3.12)$$

At the dissolution front, $y = f(x, t)$, we will have

$$v = f_t + u f_x, \quad (3.13)$$

$$u + v f_x = 0, \quad (3.14)$$

$$c = c_E(T) + \Gamma \kappa, \quad (3.15)$$

$$\frac{c}{\sqrt{1 + f_x^2}} \frac{\partial f}{\partial t} = (c\mathbf{u} - D\nabla c) \cdot \mathbf{n}_f, \quad (3.16)$$

where $\mathbf{u} = (u, v)$, \mathbf{n}_f is the unit normal vector to $y = f(x, t)$, and is given by

$$\mathbf{n}_f = \frac{1}{\sqrt{1 + f_x^2}} (-f_x, 1), \quad (3.17)$$

and κ denotes the curvature and is given by

$$\kappa = \frac{f_{xx}}{1 + f_x^2}^{3/2}. \quad (3.18)$$

Note that

- (3.15) expresses local equilibrium at the liquid–solid interface including the Gibbs–Thomson effect [9, 10], with $c_E(T)$ as the equilibrium concentration of Si at the brazing temperature, T , as given by the phase diagram and Γ as the normalized liquid–solid surface energy or solute capillary length, which is assumed to be constant;
- in (3.16), we have neglected any solid-state diffusion in the core;

– applying the Reynolds transport theorem [17] to Eq. (3.5), we find, with the help of (3.11) and (3.16) that

$$\iint_{\Omega(t)} c(x, y, t) dy dx = w_0 h_0 c_0, \quad (3.19)$$

where Ω denotes the liquid region, i.e. solute is conserved.

Furthermore, conditions are required at the contact lines, which are at $(x_1(t), 0)$ and $(0, y_1(t))$. It seems reasonable to generalize the condition derived by Warren et al. [9], and later used by Su et al. [10] and Singler et al. [18], for the contact line of an axisymmetric droplet during reactive spreading on a horizontal substrate. Warren et al. [9] assume that the contact line remains at the initial level of the substrate and that the total angle between the meniscus and the liquid–solid interface, θ_L , remains constant; in the present context, and with reference to Fig. 3,

$$\theta_{b,x_1} + \theta_{t,x_1} = \theta_L, \quad \theta_{b,y_1} + \theta_{t,y_1} = \theta_L. \quad (3.20)$$

However, since there is a discontinuity in the slope between the liquid surface and the liquid–solid interface, there will arise an additional restriction from the requirement that the liquid concentration must be well-defined and differentiable at the triple junction. The resulting expressions for the velocities of the contact lines, \dot{x}_1 and \dot{y}_1 , are

$$\dot{x}_1 = -D \left(\frac{\tan \theta_{b,x_1} + \tan \theta_{t,x_1}}{c \tan \theta_{b,x_1}} \frac{\partial c}{\partial x} \right) \Big|_{(x_1(t), 0)} = -D \Gamma \left(\frac{\tan \theta_L}{c \tan \theta_{b,x_1}} \frac{\partial \kappa}{\partial x} \right) \Big|_{(x_1(t), 0)}, \quad (3.21)$$

$$\dot{y}_1 = -D \left(\frac{\tan \theta_{b,y_1} + \tan \theta_{t,y_1}}{c \tan \theta_{b,y_1}} \frac{\partial c}{\partial y} \right) \Big|_{(0, y_1(t))} = -D \Gamma \left(\frac{\tan \theta_L}{c \tan \theta_{b,y_1}} \frac{\partial \kappa}{\partial y} \right) \Big|_{(0, y_1(t))}, \quad (3.22)$$

where the dots denote differentiation with respect to time.

In the model, θ_L is a prescribed constant—and has to be determined experimentally—but θ_{b,x_1} , θ_{t,x_1} , θ_{b,y_1} and θ_{t,y_1} are all functions of time and must all be determined. Equation (3.20) can then be written in terms of f and h as

$$\frac{h_x(0, t) - f_x(0, t)}{1 + h_x(0, t) f_x(0, t)} = \tan \theta_L, \quad (3.23)$$

$$\frac{h_x(x_1, t) - f_x(x_1, t)}{1 + h_x(x_1, t) f_x(x_1, t)} = -\tan \theta_L, \quad (3.24)$$

and further conditions are

$$f(0, t) = h(0, t), \quad (3.25)$$

$$f(x_1, t) = 0, \quad (3.26)$$

$$h(x_1, t) = 0. \quad (3.27)$$

Equations (3.25)–(3.27) are perhaps worthy of further explanation, as they are not obvious. In general, one would expect $f(x_1, t) = h(x_1, t)$, so that both the x - and y -locations of the contact are not known and have to be determined. However, Warren et al. [9] take $f(x_1, t) = 0$, $h(x_1, t) = 0$, which at least leads to a well-posed mathematical problem. On the other hand, Villanueva et al. [11] treat a similar problem using phase-field methods and obtain an elevation of the contact line relative to the $y = 0$ level, which is apparently qualitatively similar to the experimental observations of Saiz et al. [19, 20]; nevertheless, the elevation is small compared to the maximum height of the droplet, which suggests that (3.26) and (3.27) can be a suitable approximation. Thus, having adopted this approximation at the horizontal boundary, we may adopt it at the vertical one also, giving Eq. (3.25). Note that although it is written as one equation, it may be thought of as two if we write

$$f^{-1}(y_1(t), t) = 0, \quad h^{-1}(y_1(t), t) = 0, \quad (3.28)$$

where f^{-1} and h^{-1} denote the inverse functions of f and h , respectively.

The initial conditions at $t = 0$ should be

$$u = 0, \quad v = 0, \quad c = c_0 \quad \text{for } 0 < x < w_0, 0 < y < h_0, \quad (3.29)$$

$$\begin{cases} h^{-1}(y, 0) = w_0, & 0 \leq y \leq h_0, \\ h(x, 0) = h_0, & 0 \leq x \leq w_0, \end{cases} \quad (3.30)$$

$$\begin{cases} f^{-1}(y, 0) = 0, & 0 \leq y \leq h_0, \\ f(x, 0) = 0, & 0 \leq x \leq w_0. \end{cases} \quad (3.31)$$

The last of these implies that none of the cores has dissolved.

4 Nondimensionalization

The relevant length scale that should appear is the capillary length scale for the meniscus, $l = \sqrt{\sigma_{fs}/\rho g}$. Thus, we nondimensionalize with

$$X = \frac{x}{l}, \quad Y = \frac{y}{l}, \quad U = \frac{u}{[u]}, \quad V = \frac{v}{[u]},$$

$$P = \frac{p - p_a}{\sqrt{\rho g \sigma_{fs}}}, \quad \tau = \frac{t}{[t]}, \quad H = \frac{h}{l}, \quad F = \frac{f}{l},$$

where $[u]$ is a velocity scale to be determined and $[t] = l/[u]$; in fact, it turns out to be appropriate to take $[u] = D/l$, whence $[t] = l^2/D$, although we discuss the selection of $[u]$ in Appendix A. Also, for the time being, we set

$$X_1 = \frac{x_1}{l}, \quad Y_1 = \frac{y_1}{l}. \quad (4.1)$$

We obtain, from (3.2)–(3.5),

$$\frac{\partial U}{\partial X} + \frac{\partial V}{\partial Y} = 0, \quad (4.2)$$

$$Re \left(\frac{\partial U}{\partial \tau} + U \frac{\partial U}{\partial X} + V \frac{\partial U}{\partial Y} \right) = -\frac{1}{Ca} \frac{\partial P}{\partial X} + \frac{\partial^2 U}{\partial X^2} + \frac{\partial^2 U}{\partial Y^2}, \quad (4.3)$$

$$Re \left(\frac{\partial V}{\partial \tau} + U \frac{\partial V}{\partial X} + V \frac{\partial V}{\partial Y} \right) = -\frac{1}{Ca} \frac{\partial P}{\partial Y} + \frac{\partial^2 V}{\partial X^2} + \frac{\partial^2 V}{\partial Y^2} - \frac{1}{Ca}, \quad (4.4)$$

$$\frac{\partial c}{\partial \tau} + U \frac{\partial c}{\partial X} + V \frac{\partial c}{\partial Y} = \frac{\partial^2 c}{\partial X^2} + \frac{\partial^2 c}{\partial Y^2}, \quad (4.5)$$

where

$$Ca = \frac{\mu [u]}{\sigma_{fs}}, \quad Re = \frac{\rho [u] l}{\mu}; \quad (4.6)$$

these are, respectively, the capillary and Reynolds numbers. Also, conservation of mass for the clad gives

$$\int_0^{X_1(\tau)} H(X, \tau) dX = W_0 H_0, \quad (4.7)$$

where $W_0 = w_0/l$, $H_0 = h_0/l$, whereas conservation of solute for the liquid region gives

$$\int_0^{X_1(\tau)} \int_{F(X,\tau)}^{H(X,\tau)} c(X, Y, \tau) dY dX = W_0 H_0 c_0. \quad (4.8)$$

4.1 Boundary and initial conditions

Equations (3.7), (3.8), (3.10) and (3.11) give, at $Y = H(X, \tau)$,

$$2 \left(\frac{\partial V}{\partial Y} - \frac{\partial U}{\partial X} \right) H_X + \left(\frac{\partial U}{\partial Y} + \frac{\partial V}{\partial X} \right) \left\{ 1 - H_X^2 \right\} = 0, \quad (4.9)$$

$$-P + \frac{2Ca}{1 + H_X^2} \left\{ \frac{\partial U}{\partial X} H_X^2 + \frac{\partial V}{\partial Y} - \left(\frac{\partial U}{\partial Y} + \frac{\partial V}{\partial X} \right) H_X^2 \right\} = \frac{H_{XX}}{1 + H_X^2}{}^{3/2}, \quad (4.10)$$

$$V = H_\tau + U H_X, \quad (4.11)$$

$$\mathbf{n}_H \cdot \nabla c = 0, \quad (4.12)$$

respectively, where

$$\mathbf{n}_H = \frac{1}{1 + H_X^2} (-H_X, 1). \quad (4.13)$$

Equations (3.13)–(3.16) give, at $Y = F(X, \tau)$,

$$V = F_\tau + U F_X, \quad (4.14)$$

$$U + V F_X = 0, \quad (4.15)$$

$$c = c_E(T) + \frac{\delta F_{XX}}{1 + F_X^2}{}^{3/2}, \quad (4.16)$$

$$\frac{c}{1 + F_X^2} \frac{\partial F}{\partial \tau} = \mathbf{n}_F \cdot (c\mathbf{U} - \nabla c), \quad (4.17)$$

respectively, where $\mathbf{U} = (U, V)$, $\delta = \Gamma/l$ and

$$\mathbf{n}_F = \frac{1}{1 + F_X^2} (-F_X, 1). \quad (4.18)$$

At the contact lines, (3.21) and (3.22) become, respectively,

$$\dot{X}_1 = - \left(\frac{\tan \theta_{b,x_1} + \tan \theta_{t,x_1}}{c \tan \theta_{b,x_1}} \frac{\partial c}{\partial X} \right) \Big|_{(X_1(\tau), 0)} = - \left\{ \frac{\delta \tan \theta_L}{c \tan \theta_{b,x_1}} \left(\frac{F_{XX}}{1 + F_X^2}{}^{3/2} \right) \right\} \Big|_{(X_1(\tau), 0)}, \quad (4.19)$$

$$\dot{Y}_1 = - \left(\frac{\tan \theta_{b,y_1} + \tan \theta_{t,y_1}}{c \tan \theta_{b,y_1}} \frac{\partial c}{\partial Y} \right) \Big|_{(0, Y_1(\tau))} = - \left\{ \frac{\delta \tan \theta_L}{c F_X \tan \theta_{b,y_1}} \left(\frac{F_{XX}}{1 + F_X^2}{}^{3/2} \right) \right\} \Big|_{(0, Y_1(\tau))}, \quad (4.20)$$

whereas (3.23)–(3.27) give, respectively,

$$\frac{H_X(0, \tau) - F_X(0, \tau)}{1 + H_X(0, \tau) F_X(0, \tau)} = \tan \theta_L, \quad (4.21)$$

$$\frac{H_X(X_1, \tau) - F_X(X_1, \tau)}{1 + H_X(X_1, \tau) F_X(X_1, \tau)} = -\tan \theta_L, \quad (4.22)$$

$$F(0, \tau) = H(0, \tau), \quad (4.23)$$

$$F(X_1, \tau) = 0, \quad (4.24)$$

$$H(X_1, \tau) = 0. \quad (4.25)$$

Lastly, the initial conditions at $\tau = 0$ are

$$U = 0, \quad V = 0, \quad c = c_0 \quad \text{for } 0 < X < W_0, 0 < Y < H_0, \quad (4.26)$$

$$\begin{cases} H^{-1}(Y, 0) = W_0, & 0 \leq Y \leq H_0, \\ H(X, 0) = H_0, & 0 \leq X \leq W_0, \end{cases} \quad (4.27)$$

$$\begin{cases} F^{-1}(Y, 0) = 0, & 0 \leq Y \leq H_0, \\ F(X, 0) = 0, & 0 \leq X \leq W_0. \end{cases} \quad (4.28)$$

5 Analysis

In this section, we consider first in Sect. 5.1 the qualitative behaviour of the transient solution; then, in Sect. 5.2, we compute steady-state solutions.

5.1 Transient behaviour

Using the parameters in Table 1, we find that $l \approx 5$ mm, which will give

$$Ca = \frac{\mu D}{l \sigma_{fs}} \sim 10^{-10}, \quad Re = \frac{\rho D}{\mu} \sim 10^{-3}, \quad \delta \sim 10^{-7}.$$

We observe now that $Ca, Re \ll 1$, and we can consider the equations at leading order in Ca . Equations (4.3) and (4.4) reduce to just

$$\frac{\partial P}{\partial X} = 0, \quad (5.1)$$

Table 1 Model parameters

Parameter	Symbol	Value	Unit	References
Diffusion coefficient	D	10^{-9}	$\text{m}^2 \text{s}^{-1}$	[9]
Gravitational acceleration	g	9.81	m s^{-2}	–
Initial clad height	h_0	1.5×10^{-4}	m	[5]
Liquidus slope	m	6.80	$\text{wt\% } ^\circ\text{C}^{-1}$	–
Al melting temperature	T_m	660.3	$^\circ\text{C}$	–
Initial clad width	w_0	0.005	m	[5]
Solute capillary length	Γ	5×10^{-10}	m	[9]
Clad viscosity	μ	0.001	Pa s	[21]
Clad density	ρ	2650	kg m^{-3}	[21]
Surface tension	σ_{fs}	0.65	N m^{-1}	[22]

$$\frac{\partial P}{\partial Y} = -1, \quad (5.2)$$

giving

$$P = P^*(\tau) - Y, \quad (5.3)$$

where P^* is a function of τ to be determined. The only other place in the problem formulation where Ca appears is in (4.10), which, on using (5.3) gives, at leading order in Ca ,

$$\frac{H_{XX}}{1 + H_X^2} = H - P^*(\tau). \quad (5.4)$$

Although the governing equation for H appears to decouple from the rest of the formulation, this is not so significant for the transient problem, since (5.4) requires boundary conditions at $X = 0$ and $X = X_1(\tau)$ which will depend on the solutions for U , V and c , to which we turn next.

We may as well now set $P = (P^*(\tau) - Y) + CaP_1$, so that (4.2)–(4.5) become

$$\frac{\partial U}{\partial X} + \frac{\partial V}{\partial Y} = 0, \quad (5.5)$$

$$Re \left(\frac{\partial U}{\partial \tau} + U \frac{\partial U}{\partial X} + V \frac{\partial U}{\partial Y} \right) = -\frac{\partial P_1}{\partial X} + \frac{\partial^2 U}{\partial X^2} + \frac{\partial^2 U}{\partial Y^2}, \quad (5.6)$$

$$Re \left(\frac{\partial V}{\partial \tau} + U \frac{\partial V}{\partial X} + V \frac{\partial V}{\partial Y} \right) = -\frac{\partial P_1}{\partial Y} + \frac{\partial^2 V}{\partial X^2} + \frac{\partial^2 V}{\partial Y^2}, \quad (5.7)$$

$$\frac{\partial c}{\partial \tau} + U \frac{\partial c}{\partial X} + V \frac{\partial c}{\partial Y} = \frac{\partial^2 c}{\partial X^2} + \frac{\partial^2 c}{\partial Y^2}. \quad (5.8)$$

The boundary and initial conditions, (4.9)–(4.28), are unchanged, apart from (4.10), which becomes

$$-P_1 + \frac{2}{1 + H_X^2} \left\{ \frac{\partial U}{\partial X} H_X^2 + \frac{\partial V}{\partial Y} - \left(\frac{\partial U}{\partial Y} + \frac{\partial V}{\partial X} \right) H_X^2 \right\} = 0. \quad (5.9)$$

Note that since $\delta \ll 1$, we can expect from (4.19) and (4.20) that $\dot{X}_1 \approx 0$, $\dot{Y}_1 \approx 0$, respectively, and then that the problem for U , V , P_1 would have the trivial solution, but for the fact that $F_\tau \neq 0$ at $Y = F(X, \tau)$; thus, the movement of the reaction front drives the velocity field in the melt via the boundary condition at $Y = F(X, \tau)$. Whilst this is true for intermediate times, prior to the steady state which we shall consider shortly, there is an additional complication concerning (4.19) and (4.20). Since θ_{b,x_1} and θ_{b,y_1} are initially zero, it is clear that the simplification that $\dot{X}_1 \approx 0$, $\dot{Y}_1 \approx 0$ will only become valid once $\theta_{b,x_1}, \theta_{b,y_1} \gg \delta$; further analysis would be required to determine a time scale for when this happens, and we do not consider it any further here.

Moreover, since \dot{X}_1 and \dot{Y}_1 are initially very large, i.e. when $\theta_{b,x_1}, \theta_{b,y_1} \ll \delta$, this stage is often identified in droplet spreading situations as that of the initial fast hydrodynamic spreading of the liquid, during which very little dissolution takes place [9]. Another interesting point is that once $\dot{X}_1 \approx 0$, $\dot{Y}_1 \approx 0$, the two contact lines stop moving; thereafter, the meniscus adjusts its profile in order that (4.21) and (4.22) are satisfied, but its endpoints are fixed.

Recalling that l^2/D was determined in Sect. 4 as the timescale for the dissolution problem, we can now attempt to infer the order of magnitude of the time required to reach steady state. Using the parameters from Table 1, l^2/D would correspond to around 25,000 s, i.e. around 7 h. Nevertheless, it needs to be emphasized that this value may be a severe overestimation. For example, if the meniscus has equal extents of $O(\mathcal{L})$ in x - and y -directions, then we should have $\mathcal{L}^2 \sim w_0 h_0$, and the relevant time scale will be \mathcal{L}^2/D . With $\mathcal{L} \sim (w_0 h_0)^{1/2} \sim 900 \mu\text{m}$, we would

obtain $\mathcal{L} \sim 750$ s, which compares well with the length of about 5 minutes of the dwell time during an optimized brazing cycle, e.g. see Fig. 3 in [4]. In practice, a full numerical simulation would be necessary to determine when the transient model reaches a steady state.

5.2 Steady state

Having identified how the transient problem as a whole operates qualitatively, we proceed to determine the steady state quantitatively. First, we note that, at steady state, $U, V, P_1 \equiv 0$ and c is constant, so that (5.5)–(5.8) are satisfied automatically, as are boundary conditions (4.9), (4.11), (4.12), (4.14), (4.15), (4.17), (4.19) and (4.20). We recall that boundary condition (4.10) resulted in Eq. (5.4), so that if we now set $\mathcal{C}_1 = -P^*(\infty)$, where \mathcal{C}_1 is a constant whose value will need to determine, we will have

$$\frac{H_{XX}}{1 + H_X^2}{}^{3/2} = H + \mathcal{C}_1. \quad (5.10)$$

Also, boundary condition (4.16) gives

$$\frac{\delta F_{XX}}{1 + F_X^2}{}^{3/2} = C_2^* - c_E(T), \quad (5.11)$$

where C_2^* is the constant steady-state value of c , which is as yet unknown; note here that even though $\delta \ll 1$, whereas $c_E(T)$ is nominally $O(1)$, the term on the right-hand side of (5.11) is critical to what follows, and is therefore not neglected. Equations (5.10) and (5.11) are subject to (4.7), (4.8) and (4.21)–(4.25), which are now, respectively,

$$\int_0^{X_*} H(X) dX = \mathcal{A}, \quad (5.12)$$

$$C_2^* \left\{ \int_0^{X_*} (H(X) - F(X)) dX \right. = c_0 \mathcal{A}, \quad (5.13)$$

$$H(0) = Y_*, \quad (5.14)$$

$$\frac{H_X(0) - F_X(0)}{1 + H_X(0)F_X(0)} = \tan \theta_L, \quad (5.15)$$

$$H(X_*) = 0, \quad (5.16)$$

$$F(X_*) = 0, \quad (5.17)$$

$$\frac{H_X(X_*) - F_X(X_*)}{1 + H_X(X_*)F_X(X_*)} = -\tan \theta_L, \quad (5.18)$$

where

$$\mathcal{A} = \frac{\rho g w_0 h_0}{\sigma_{fs}}, \quad (5.19)$$

also, $X_* = X_1(\infty)$, $Y_* = Y_1(\infty)$.

The equations can be simplified further by recalling that $\delta \ll 1$, so that $C_2^* = c_E(T) + O(\delta)$. Setting

$$C_2^* = c_E(T) + \delta \mathcal{C}_2 + O(\delta^2), \quad (5.20)$$

we see that (5.11) becomes

$$\frac{F_{XX}}{1 + F_X^2}^{3/2} = C_2, \quad (5.21)$$

whereas (5.13) simplifies to

$$\int_0^{X_*} F(X) dX = \left(\frac{c_E(T) - c_0}{c_E(T)} \right) \mathcal{A}. \quad (5.22)$$

At this stage, we have

$$\frac{H_{XX}}{1 + H_X^2}^{3/2} = H + C_1, \quad (5.23)$$

$$\frac{F_{XX}}{1 + F_X^2}^{3/2} = C_2, \quad (5.24)$$

subject to

$$H(0) = F(0), \quad (5.25)$$

$$\frac{H_X(0) - F_X(0)}{1 + H_X(0)F_X(0)} = \tan \theta_L, \quad (5.26)$$

$$H(X_*) = 0, \quad (5.27)$$

$$F(X_*) = 0, \quad (5.28)$$

$$\frac{H_X(X_*) - F_X(X_*)}{1 + H_X(X_*)F_X(X_*)} = -\tan \theta_L, \quad (5.29)$$

$$\int_0^{X_*} H(X) dX = \mathcal{A}, \quad (5.30)$$

$$\int_0^{X_*} F(X) dX = \left(\frac{c_E(T) - c_0}{c_E(T)} \right) \mathcal{A}. \quad (5.31)$$

We observe that (5.24) implies that the curvature of the curve describing the dissolved zone is constant, and it is tempting to infer that F will describe the arc of a circle in the core from $(0, Y_*)$ to $(X_*, 0)$. However, it will be shown that this cannot in general be the case. The easiest way to see this is to consider what happens when $\varepsilon := (c_0 - c_E(T)) / c_E(T) \ll 1$, although this is relegated to Appendix B; in addition, in Appendix C, it is shown that, even in the general case when $\varepsilon \sim O(1)$, there cannot be a circular arc from $(0, Y_*)$ to $(X_*, 0)$. Instead, the only resolution appears to be that there are two circular arcs, one starting at $(0, Y_*)$ and the other at $(X_*, 0)$, both of which pass through $(0,0)$ and have the same radius. Thence, we append

$$F(0) = 0 \quad (5.32)$$

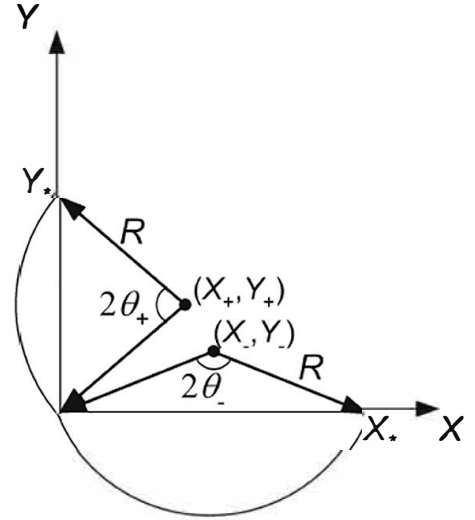
to Eqs. (5.25)–(5.31) and proceed by considering the case $\varepsilon \sim O(1)$.

We consider the circles

$$(X - X_+)^2 + (Y - Y_+)^2 = R^2, \quad (5.33)$$

$$(X - X_-)^2 + (Y - Y_-)^2 = R^2, \quad (5.34)$$

Fig. 4 Schematic for determining the extent of the dissolved region by finding the centres and radii of two circles



where X_+ , Y_+ , X_- , Y_- and R must be determined; we will later set $Y = F$. Equation (5.33) will represent a circle of radius R and having its centre at (X_+, Y_+) that passes through $(0,0)$ and $(0, Y_*)$, whereas Eq. (5.34) will represent a circle of radius R and having its centre at (X_-, Y_-) that passes through $(0,0)$ and $(X_*, 0)$; this is summarized schematically in Fig. 4. From (5.25),(5.28) and (5.32) twice, we must have

$$X_+^2 + (Y_* - Y_+)^2 = R^2, \quad (5.35)$$

$$(X_* - X_-)^2 + Y_-^2 = R^2, \quad (5.36)$$

$$X_+^2 + Y_+^2 = R^2, \quad (5.37)$$

$$X_-^2 + Y_-^2 = R^2, \quad (5.38)$$

respectively; note that (5.32) is used twice since both circular arcs must satisfy it. We quickly see that

$$Y_+^2 = (Y_* - Y_+)^2, \quad X_-^2 = (X_* - X_-)^2, \quad (5.39)$$

and hence

$$X_- = \frac{X_*}{2}, \quad Y_+ = \frac{Y_*}{2}. \quad (5.40)$$

Also,

$$X_+^2 + \frac{Y_*^2}{4} = R^2, \quad (5.41)$$

$$\frac{Y_*^2}{4} + Y_-^2 = R^2, \quad (5.42)$$

but with X_+ , Y_- and R still unknown. A further relation comes from (5.31), which gives

$$R^2\theta_+ - X_+Y_+ + R^2\theta_- - X_-Y_- = \varepsilon A. \quad (5.43)$$

where

$$\tan \theta_+ = \frac{Y_+}{X_+}, \quad \tan \theta_- = \frac{X_-}{Y_-}. \quad (5.44)$$

So,

$$R^2 (\theta_+ + \theta_-) - X_+ Y_+ - X_- Y_- = \varepsilon \mathcal{A}, \quad (5.45)$$

i.e.

$$\begin{aligned} R^2 \left(\tan^{-1} \left(\frac{Y_*}{4R^2 - Y_*^2} \right) + \tan^{-1} \left(\frac{(4R^2 - X_*^2)^{1/2}}{X_*} \right) \right) \\ - \frac{Y_*}{2} \left(R^2 - \frac{Y_*^2}{4} \right)^{1/2} - \frac{X_*}{2} \left(R^2 - \frac{X_*^2}{4} \right)^{1/2} = \varepsilon \mathcal{A}, \end{aligned} \quad (5.46)$$

which is a relation for R in terms of X_* and Y_* .

We use (5.33) and (5.34) to simplify (5.26) and (5.29). First, we see from differentiating (5.33) that

$$(X - X_+) + (Y - Y_+) \frac{dY}{dX} = 0, \quad (5.47)$$

whence, on setting $Y = F(X)$, we obtain

$$F_X(0) = \frac{2X_+}{Y_*}. \quad (5.48)$$

From (5.34),

$$(X - X_-) + (Y - Y_-) \frac{dY}{dX} = 0, \quad (5.49)$$

whence, similarly,

$$F_X(X_*) = \frac{X_*}{2Y_-}. \quad (5.50)$$

Now, we can re-arrange (5.26) and (5.29) to obtain

$$H_X(0) = \frac{F_X(0) + \tan \theta_L}{1 - F_X(0) \tan \theta_L}, \quad (5.51)$$

$$H_X(X_*) = \frac{F_X(X_*) - \tan \theta_L}{1 + F_X(X_*) \tan \theta_L}, \quad (5.52)$$

respectively, and hence

$$H_X(0) = \frac{2X_+ + Y_* \tan \theta_L}{Y_* - 2X_+ \tan \theta_L}, \quad (5.53)$$

$$H_X(X_*) = \frac{X_* - 2Y_- \tan \theta_L}{2Y_- + X_* \tan \theta_L}, \quad (5.54)$$

where

$$X_+ = \left(R^2 - \frac{Y_*^2}{4} \right)^{1/2}, \quad Y_- = \left(R^2 - \frac{X_*^2}{4} \right)^{1/2}, \quad (5.55)$$

and with R given by the solution to Eq. (5.46).

A further interesting observation in relation to earlier work concerns the function H , rather than F . Terrill [1] approximated the meniscus of a tee joint with a quarter of a circle. This would mean neglecting the term in H on the right-hand side of (5.23), leaving us with an equation that is qualitatively similar to (5.24), with the end result being just a meniscus having constant curvature. However, it is clear from the analysis that the term in H is a leading-order term in the model, and should therefore not be neglected.

5.3 Model summary and numerical solution

The model equations have been reduced to just one nonlinear second-order ordinary differential equation, (5.23), subject to (5.27), (5.30), (5.46), (5.53) and (5.54), with the unknowns being H, R, X_* and C_1 ; there are thus five constraints for five unknowns, with the latter being R, X_*, C_1 and the two constants of integration from (5.23). Once, these are determined, X_+, Y_+, Y_* and C_2 can be found.

Although it is a computationally inexpensive task to solve these equations, some care is necessary in finding a suitable initial guess for H, R, X_* and C_1 ; a poor guess leads to the square root of negative numbers in (5.46). Thereafter, once a solution is found for one (θ_L, ε) -combination, it can be used as the initial guess for finding solutions for other combinations by parameter stepping. Moreover, although what we have is a boundary-value problem, the location of one of the boundaries, $X = X_*$, is not known beforehand. It is therefore convenient to use boundary immobilization, and this is done by introducing the variables \hat{X} and \hat{H} , which are given by

$$X = X_* \hat{X}, \quad H = X_* \hat{H}, \quad (5.56)$$

leading to, for $0 \leq \hat{X} \leq 1$,

$$\frac{\hat{H}_{\hat{X}\hat{X}}}{(1 + \hat{H}_{\hat{X}}^2)^{3/2}} = X_* (X_* \hat{H} + C_1), \quad (5.57)$$

subject to

$$\hat{H}(1) = 0, \quad (5.58)$$

$$X_*^2 \int_0^{X_*} \hat{H}(X) dX = \mathcal{A}, \quad (5.59)$$

$$\hat{H}_{\hat{X}}(0) = \frac{2X_+ + Y_* \tan \theta_L}{Y_* - 2X_+ \tan \theta_L}, \quad (5.60)$$

$$\hat{H}_{\hat{X}}(1) = \frac{X_* - 2Y_- \tan \theta_L}{2Y_- + X_* \tan \theta_L}, \quad (5.61)$$

and (5.46), where $Y_* = X_* \hat{H}(0)$. These equations were solved using the finite element software Comsol Multiphysics, typically using a few hundred elements to discretize the interval $0 \leq \hat{X} \leq 1$. It is straightforward to ensure that the results are mesh-independent, and we do not document those calculations here.

6 Results

To validate the model, data paralleling the experimental details given by Sekulic [5] were considered. The core alloy consists of AA3003 alloy which is mainly an Al–Mn alloy with 1.1–1.5 wt% Mn and little Fe and Si. The clad alloy is a AA4343 alloy with 8 wt% Si, 0.8 wt% Fe, 0.25 wt% Cu, 0.10 wt% Mn and 0.20 wt% Zn (in wt.%), and has a liquidus of 607.8 °C, as calculated using the TCAL2 database [23]. The thickness of the clad was $w_0 = 200\mu\text{m}$. Heating to the brazing upper temperature and cooling from it were both performed at a rate higher than 50 °C/min, which would be large enough that solid-state diffusion of silicon does not affect the amount of clad available [16]. Although Sekulic [5] indicates an upper brazing temperature of 600 °C for the experiment he reported, he implicitly assumed in his approach that all the clad had melted. Indeed, brazing for 3003/4343 assemblies may be performed from 600 to 615 °C [24], i.e. from slightly below to slightly above the clad liquidus temperature.

In the present modelling approach, the clad alloy is considered as a binary Al–Si alloy, the liquidus temperature of which is estimated as $T_m - mc_0$, where the values for T_m and m are as given in Table 1. As for c_0 , we note that if we take 8 wt% Si, as indicated above, this would imply a value lower than that of c_E at 600 °C, which is 8.8 wt% Si; this would give $\varepsilon < 0$. On the other hand, if we sum up the non-Al compositions given above and assign this sum to be c_0 , then we obtain 9.4 wt% Si, giving $\varepsilon > 0$. Since the model is only self-consistent if $\varepsilon \geq 0$, we will therefore take $c_0 = 9.4\text{ wt\%}$.

At this stage, we still need to prescribe h_0 and θ_L . To calculate h_0 , we use Fig. 3(b) and (c) from [5], which indicate the cross-sectional area of the joint to be $7.060 \times 10^{-7}\text{ m}^2$ and $6.423 \times 10^{-7}\text{ m}^2$; using these and the value of w_0 given above leads to $h_0 = 3.53 \times 10^{-3}\text{ m}$ and $3.21 \times 10^{-3}\text{ m}$, respectively. As for θ_L , this is a quantity that does not explicitly appear at all in [5], where it is argued that the fact that a good brazed joint indicates a very small inclination angle of the joint surface close to the mating surfaces implies that an assumption of a close-to-zero contact angle between the molten metal and the solid substrate at the onset of solidification is plausible indeed. Here, we will keep θ_L as a parameter, the value of which we will vary, thereby seeing what effect it has on the solution.

Moving to the results, Figs. 5 and 6 compare the experimental results from Fig. 3(b) and (c), respectively, in [5] with our model results for $\theta_L = 0.05, 0.07$ and 0.09 , corresponding to $2.86^\circ, 4.01^\circ$ and 5.16° , respectively; for these, $\varepsilon = 0.06$. From this, it is notable the all three model curves agree reasonably well with the experimental data, although the height of the meniscus is somewhat underpredicted towards $x = 0$ in Fig. 5; this was also a feature of the model results in [5]. Also of note is the fact that the predicted profile is insensitive to θ_L as its value is increased from 0.05 to 0.09; consequently, even though we may not have a way to determine θ_L , it is not much of consequence. This may lead us to believe that we should simply set $\theta_L = 0$. However, an interesting theoretical result that can even be obtained analytically in this case is that the contact line can extend to infinity in the zero-dissolution limit,

Fig. 5 Comparison of experimental data from Fig. 3(b) in [5] with the meniscus profile, h , computed using the current model with $\theta_L = 0.05, 0.07, 0.09$ and $\varepsilon = 0.06$. Note that the curves for $\theta_L = 0.05, 0.07, 0.09$ are literally on top of each other

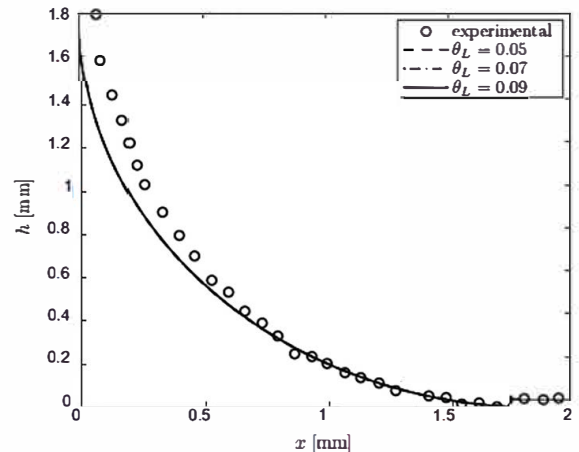


Fig. 6 Comparison of experimental data from Fig. 3(c) in [5] with the meniscus profile, h , computed using the current model with $\theta_L = 0.05, 0.07, 0.09$ and $\varepsilon = 0.06$. Note that the curves for $\theta_L = 0.05, 0.07, 0.09$ are literally on top of each other

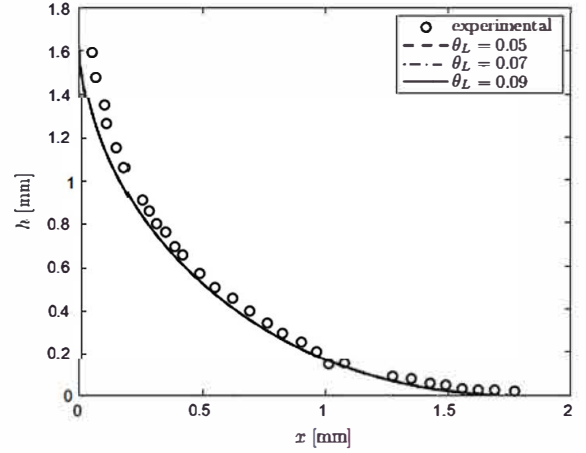
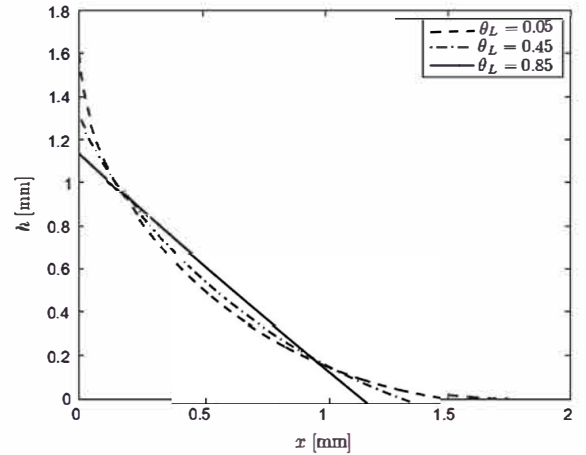


Fig. 7 Meniscus profile, h , vs. x ($\theta_L = 0.05, 0.45, 0.85$)



$\varepsilon = 0$; this is explained in detail in Appendix D. Moreover, we also found that, in our model, it became no longer possible to obtain converged solutions for values of θ_L lower than around 0.044; this was in spite of the fact that we use the best available initial guesses for the solution at each value of θ_L . This behaviour is no doubt due to the fact that $\varepsilon > 0$; there was no problem at all to find solutions in the limit as $\theta_L \rightarrow 0$ for $\varepsilon = 0$, and indeed there is even an analytical solution in this case, as shown by Eq. (D.12) in Appendix D.

Although the above results might suggest that the solution is more or less independent of θ_L , this is not the case, and its value can affect the meniscus profile. To see this, consider Fig. 7 wherein values have been computed as $\theta_L = 0.05, 0.45$, and 0.85 , corresponding, respectively, to $5.16^\circ, 25.78^\circ$ and 48.70° , for $\varepsilon = 0.06$, and the same cross-sectional area as for Fig. 6; hence, as θ_L is increased, the profile becomes almost linear, and hence far-removed from the experimental observations.

Lastly, we consider how varying the value of ε affects the solution. Figure 8 shows the profiles for f and h for $\varepsilon = 0.44, 0.74$ and 1.04 , corresponding to temperatures of $614.8^\circ\text{C}, 622.6^\circ\text{C}$ and 628.1°C , respectively; $\theta_L = 0.85$, corresponding to 48.70° ; and a cross-sectional area of $7.060 \times 10^{-7} \text{ m}^2$. These values of ε and θ_L have been chosen arbitrarily, and are sufficiently different from the values used for Figs. 5 and 6 so as to illustrate that the model works for a wide range of parameters. In this case, we see that, even though we have chosen a high value of θ_L , the profiles for h are qualitatively reasonable, and do not resemble the linear profile in Fig. 7. This is of course in part due to the fact that there is now a significant dissolved region, with the f -profile being responsible for a greater share of θ_L than the h -profile.

7 Conclusions

In this paper, we have considered a framework for the mathematical modelling of reactive wetting during brazing; more specifically, a simplified 2D inverted tee-joint geometry consisting of an unclad horizontal plate and a vertical plate with cladding was considered. The key points are as follows:

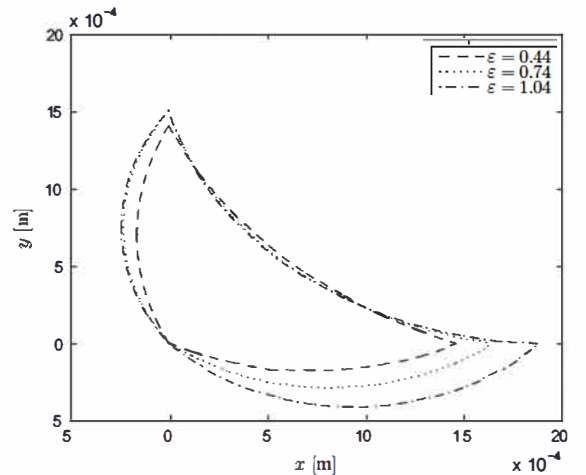
1. Once the clad is molten, the problem bears some similarity to those of the reactive wetting that occurs during the spread of a molten droplet, as has been considered by others [9, 10, 18].
2. Although it is a challenging mathematical problem to determine the time evolution of the molten clad meniscus and the dissolution front that forms, it is much easier to determine the theoretical steady state, and this was done here; the standout plot for this is Fig. 8, which shows the steady-state profiles for the meniscus and dissolved region for three different brazing temperatures, assuming a prescribed value for the angle, θ_L , between the meniscus and the dissolution front. This constitutes the maximum possible spatial extent of the dissolved zone.
3. Moreover, there exists a simple approximate relation between the area of the dissolved zone (A_{diss}), the initial amount of clad ($w_0 h_0$), the equilibrium concentration of Si at the brazing temperature ($c_E(T)$) and the initial composition of the clad, c_0 :

$$A_{diss} = w_0 h_0 \left(\frac{c_0}{c_E(T)} - 1 \right). \quad (7.1)$$

Possible directions for further modelling work would involve the following:

- computation of the time evolution of the meniscus and the dissolved region towards a steady state. The problem of a T-joint is considerably more complicated than that of the spreading droplet because there are two contact lines to consider and the use of so-called “lubrication theory” that is highlighted in [9, 10, 18] is no longer strictly speaking valid since the aspect ratio of the molten region is not small. Another possibility, although computationally more challenging, is the use of a phase-field approach [11–13], which involves the use of a particular type of diffuse-interface model that is based on the free energy as a function of state variables; this has the benefit, at least, that the force singularity which arises in the classical model of moving contact lines, first pointed out by Huh and Scriven [25], is no longer present due to mass transfer across the interface [26]. In this context, we can note that the model we have presented here would indeed lead to such a singularity, although it could be alleviated by introducing a slip coefficient into the no-slip boundary condition, as has previously been done by many others, e.g. [27]. Yet another possibility is to use a sharp-interface method via an Arbitrary

Fig. 8 f and h ($\theta_L = 0.85$, corresponding to 48.70° , and $\varepsilon = 0.44, 0.74, 1.04$), obtained not using the assumption that $\varepsilon \ll 1$



Lagrangian Eulerian (ALE) formulation; interestingly, ALE also appears to have been used by others [18,28]. There do exist even simpler models based around the Noyes–Whitney equation [29].

- consideration of how the model differs if the brazing temperature T is such that $T < T_m - mc_0$. In this case, the clad is only partly molten, and therefore not all of it is available for flow. Hence, there will be a mushy zone and a Darcy-law term needs to be added to the Navier–Stokes equation. Moreover, it is evident that, although $\varepsilon > 0$ when all of the clad is molten, we will now have $\varepsilon < 0$. When $\varepsilon > 0$, it is clear that it gives a characteristic scale for the extent of the dissolved region; on the other hand, if $\varepsilon < 0$, the interpretation is far less straightforward, since not all of the clad will have melted.

Acknowledgements The first author acknowledges the award of a visiting researcher grant from FAPESP (Fundação de Amparo à Pesquisa do Estado de São Paulo) [Grant Number 2018/07643-8]. Both authors would like to thank the anonymous referees for their constructive comments.

Appendix A: Determining the velocity scale, $[u]$

In addition to $[u] = D/l$, another possibility is to take $[u] = D\Gamma/l^2$. In this case, we have

$$[t] = \frac{l}{[u]} = \frac{l^3}{D\Gamma}, \quad (\text{A.1})$$

and (4.19) and (4.20) become

$$\dot{X}_1 = - \left\{ \frac{\tan \theta_L}{c \tan \theta_{b,x_1}} \left(\frac{F_{XX}}{1 + F_X^2} \right)^{3/2} \right\}_X \Big|_{(X_1(\tau), 0)}, \quad (\text{A.2})$$

$$\dot{Y}_1 = - \left\{ \frac{\tan \theta_L}{c \tan \theta_{b,y_1}} \left(\frac{F_{XX}}{1 + F_X^2} \right)^{3/2} \right\}_X \Big|_{(0, Y_1(\tau))}, \quad (\text{A.3})$$

respectively. Also, (4.5) and (4.17) become

$$\frac{\partial c}{\partial \tau} + U \frac{\partial c}{\partial X} + V \frac{\partial c}{\partial Y} = \frac{1}{\delta} \left(\frac{\partial^2 c}{\partial X^2} + \frac{\partial^2 c}{\partial Y^2} \right), \quad (\text{A.4})$$

$$-\frac{\delta c}{1 + F_X^2} \frac{\partial F}{\partial \tau} = \mathbf{n}_F \cdot (c\mathbf{u} - D\nabla c) \quad \text{at } Y = F(X, \tau), \quad (\text{A.5})$$

respectively. It is now convenient to refer to Table 1, which contains the model parameters. Now, since $\delta \ll 1$, (A.4) and (A.5) reduce to

$$\frac{\partial^2 c}{\partial X^2} + \frac{\partial^2 c}{\partial Y^2} \approx 0, \quad (\text{A.6})$$

$$\mathbf{n}_F \cdot \nabla c \approx 0 \quad \text{at } Y = F(X, \tau); \quad (\text{A.7})$$

i.e. this is already the steady state. Also, from (A.1), we would obtain $[t] \sim 10^{10}$ s, and it is clear that we must have taken the wrong choice for $[u]$.

Appendix B: $\varepsilon \ll 1$

In this case, the F and H problems decouple in an interesting way. From (5.31), and assuming that $\mathcal{A} \sim O(1)$, we now expect that

$$\int_0^{X_*} F(X) dX \sim O(\varepsilon). \quad (\text{B.1})$$

For $Y < 0$, this should mean that $X \sim O(1)$, $F \sim O(\varepsilon)$, whereas for $Y > 0$, we expect $F \sim O(1)$ when $X \sim O(\varepsilon)$.

Considering the first case, if $F = \varepsilon \bar{F}$, with the expectation that \bar{F} is an $O(1)$ function, implies that (5.24) becomes, at leading order in ε ,

$$\frac{d^2 \bar{F}}{dX^2} = \bar{C}_2, \quad (\text{B.2})$$

where $C_2 = \bar{C}_2/\varepsilon$, with \bar{C}_2 an $O(1)$ constant, whereas (5.28) and (5.29) reduce to

$$\bar{F}(X_*) = 0, \quad (\text{B.3})$$

$$H_X(X_*) = -\tan \theta_L, \quad (\text{B.4})$$

respectively. For the second case, we set $X = \varepsilon \bar{X}$, so that (5.24) becomes

$$\frac{d^2 F}{d\bar{X}^2} = \bar{C}_2 \left(\frac{dF}{d\bar{X}} \right)^3, \quad (\text{B.5})$$

with (5.26) reducing to

$$H_X(0) = -\cot \theta_L. \quad (\text{B.6})$$

Note that, at this stage, (B.2) and (B.5) are consistent with each other, and the implication is that the radius of curvature of F , which is in effect $1/C_2$, is small. Also, we can note that the problem for H has now decoupled from that for F . More specifically, we have, for H , Eq. (5.23) subject to

$$H_X(0) = -\cot \theta_L, \quad (\text{B.7})$$

$$H(X_*) = 0, \quad (\text{B.8})$$

$$H_X(X_*) = -\tan \theta_L, \quad (\text{B.9})$$

$$\int_0^{X_*} H(X) dX = \mathcal{A}; \quad (\text{B.10})$$

so, there are enough constraints to determine H , C_1 and X_* , and thus $H(0)$.

Returning to the problem for F , we have

$$\frac{d^2 \bar{F}}{dX^2} = \bar{C}_2, \quad (\text{B.11})$$

subject to

$$\bar{F}(X_*) = 0, \quad (\text{B.12})$$

and

$$\frac{d^2 F}{d\bar{X}^2} = \bar{C}_2 \left(\frac{dF}{d\bar{X}} \right)^3, \quad (\text{B.13})$$

subject to

$$F(0) = H(0). \quad (\text{B.14})$$

Each of these problems is clearly missing a boundary condition, and hence two more conditions would be required. One would hope for continuity of F and its derivative, so that the two problems would “join up”, in the sense that F and dF/dX as computed by the two problems should be continuous at some value of X that would have to be determined. However, it is impossible to achieve this, whilst at the same time ensuring that the curvature of F is constant. Thus, the only apparent possibility is that

$$F(0) = 0, \quad (\text{B.15})$$

and hence that

$$\bar{F}(0) = 0, \quad (\text{B.16})$$

which abandons the requirement that dF/dX is continuous. In this case, dissolution does not start at all from the point $(0,0)$. Note that (B.15) will mean that F is multivalued at $X = 0$, and indeed for $X < 0$.

The remaining problem for \bar{F} is (B.11), subject to (B.12) and (B.16), and we obtain

$$\bar{F} = \frac{1}{2} \bar{C}_2 X (X - X_*). \quad (\text{B.17})$$

The remaining problem for F is (B.13), subject to (B.14) and (B.15). To solve, it is easier to rewrite the problem as

$$\frac{d^2 \bar{X}}{dF^2} = \bar{C}_2, \quad (\text{B.18})$$

subject to

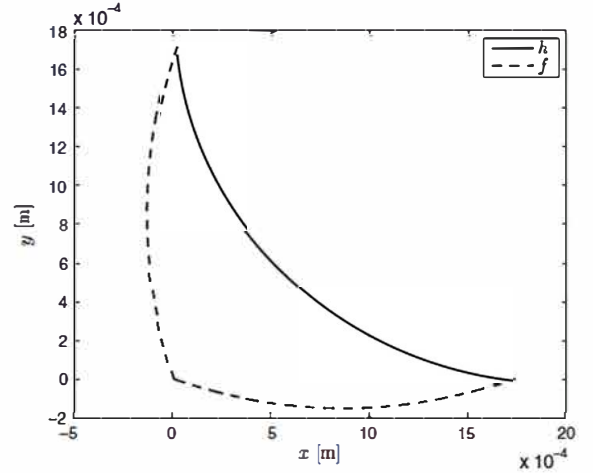
$$\bar{X}(0) = 0, \quad (\text{B.19})$$

$$\bar{X}(Y_*) = 0, \quad (\text{B.20})$$

which leads to the solution

$$\bar{X} = -\frac{1}{2} \bar{C}_2 F (F - Y_*). \quad (\text{B.21})$$

Fig. 9 f and h
 $(\theta_L = 0.1, \varepsilon = 0.445)$,
obtained using the
assumption that $\varepsilon \ll 1$



Finally, \bar{C}_2 will be given from (5.31) by

$$\frac{1}{2}\bar{C}_2 \int_0^{X_*} X(X_* - X) dX + \frac{1}{2}\bar{C}_2 \int_0^{Y_*} F(Y_* - F) dF = \mathcal{A}, \quad (\text{B.22})$$

leading to

$$\bar{C}_2 = \frac{12\mathcal{A}}{X_*^3 + Y_*^3}. \quad (\text{B.23})$$

So,

$$F = \begin{cases} \frac{1}{2}\varepsilon\bar{C}_2 X(X - X_*) & X > 0, \\ \frac{1}{2} \left\{ Y_* \pm \sqrt{Y_*^2 + \frac{8\varepsilon}{\bar{C}_2} X} \right\} & X < 0. \end{cases} \quad (\text{B.24})$$

A preliminary result for f and h is given in Fig. 9 using $\theta_L = 0.1$ (5.71°) and $T = 615^\circ\text{C}$, corresponding to $\varepsilon = 0.445$. Note that the sum of the area in $y < 0$ and $x < 0$ should be 0.445 that in $x, y, > 0$.

Furthermore, Fig. 10 shows the extent of the dissolution zone for $T = 595^\circ\text{C}$, 615°C and 625°C . Note that the curve for $T = 595^\circ\text{C}$ is literally on top of the x - and y -axes. For this $\varepsilon \ll 1$ analysis, these curves are calculated using the results from the $O(1)$ problem for H ; thus, X_* and Y_* are the same for all of these curves.

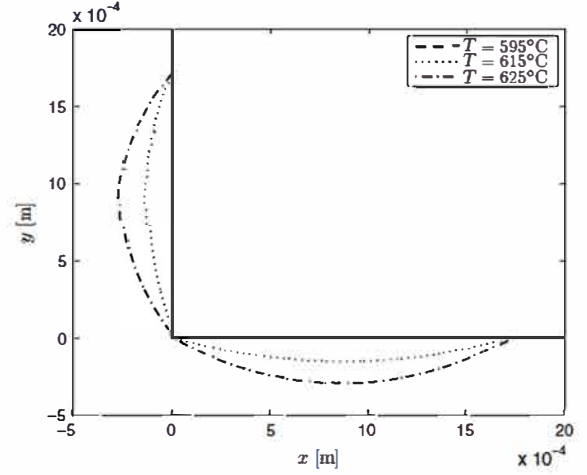
Appendix C: A one-circle dissolution zone for $\varepsilon \ll 1$?

It was seen in Appendix B that if $\varepsilon \ll 1$, then it is not possible that a single circular arc will join the two contact lines. However, it is not yet clear that this is the case if ε is larger, as will be the case when the difference between c_0 and $c_E(T)$ is large, or $c_E(T)$ is sufficiently small. Thus, we now consider this situation.

Suppose that such a circular arc exists and that it is part of the circle

$$(X - X_0)^2 + (Y - Y_0)^2 = R^2, \quad (\text{C.1})$$

Fig. 10 f ($\theta_L = 0.1$,
 $T = 595^\circ\text{C}$, 615°C ,
 625°C), obtained using the
assumption that $\varepsilon \ll 1$



where X_0 , Y_0 and R are to be determined; then we would need

$$X_0^2 + (Y_* - Y_0)^2 = R^2, \quad (\text{C.2})$$

$$(X_* - X_0)^2 + Y_0^2 = R^2. \quad (\text{C.3})$$

Also, since

$$(X - X_0) + (Y - Y_0) \frac{dY}{dX} = 0, \quad (\text{C.4})$$

we have

$$F_X(0) = \frac{X_0}{Y_* - Y_0}, \quad F_X(X_*) = \frac{X_* - X_0}{Y_0}. \quad (\text{C.5})$$

We observe that

$$X_0^2 + (Y_* - Y_0)^2 = (X_* - X_0)^2 + Y_0^2, \quad (\text{C.6})$$

which gives

$$Y_*^2 - 2Y_*Y_0 = X_*^2 - 2X_*X_0, \quad (\text{C.7})$$

whence

$$Y_0 = \frac{Y_*^2 - X_*^2 + 2X_*X_0}{2Y_*}. \quad (\text{C.8})$$

Also,

$$\frac{1}{\gamma}R^2\theta - X_0Y_0 - \frac{1}{\gamma}X_0(Y_* - Y_0) - \frac{1}{\gamma}Y_0(X_* - X_0) = \varepsilon\mathcal{A}. \quad (\text{C.9})$$

where

$$\theta = \frac{\pi}{2} + \tan^{-1} \left(\frac{Y_* - Y_0}{X_0} \right) + \tan^{-1} \left(\frac{X_* - X_0}{Y_0} \right); \quad (\text{C.10})$$

here, (C.9) comes from Eq. (5.31), i.e. the conservation of solute condition.

Numerical experimentation to determine f and h indicated that there are not only great difficulties in finding a numerical solution, but also difficulties in finding a good initial guess; it is necessary to find this because the governing equations are nonlinear. Moreover, it is not even known if a solution exists. Thus, it turns out to be more worthwhile to consider what would be the properties of such a solution, if it exists. We know that we must have

$$H_X(0) = \frac{X_0 + (Y_* - Y_0) \tan \theta_L}{Y_* - Y_0 - X_0 \tan \theta_L}, \quad (\text{C.11})$$

$$H_X(X_*) = \frac{X_* - X_0 - Y_0 \tan \theta_L}{Y_0 + (X_* - X_0) \tan \theta_L}, \quad (\text{C.12})$$

which we can rewrite as

$$X_0 + (Y_* - Y_0) \tan \theta_L = (Y_* - Y_0 - X_0 \tan \theta_L) H_X(0), \quad (\text{C.13})$$

$$X_* - X_0 - Y_0 \tan \theta_L = (Y_0 + (X_* - X_0) \tan \theta_L) H_X(X_*), \quad (\text{C.14})$$

i.e.

$$\begin{pmatrix} a & b \\ c & d \end{pmatrix} \begin{pmatrix} X_0 \\ Y_0 \end{pmatrix} = \begin{pmatrix} e \\ f \end{pmatrix}, \quad (\text{C.15})$$

where

$$a = 1 + H_X(0) \tan \theta_L, \quad (\text{C.16})$$

$$b = H_X(0) - \tan \theta_L, \quad (\text{C.17})$$

$$c = H_X(X_*) \tan \theta_L - 1, \quad (\text{C.18})$$

$$d = -H_X(X_*) - \tan \theta_L, \quad (\text{C.19})$$

$$e = Y_* (H_X(0) - \tan \theta_L), \quad (\text{C.20})$$

$$f = X_* (H_X(X_*) \tan \theta_L - 1), \quad (\text{C.21})$$

so that

$$\begin{pmatrix} X_0 \\ Y_0 \end{pmatrix} = \frac{1}{ad - bc} \begin{pmatrix} de - bf \\ -ce + af \end{pmatrix}. \quad (\text{C.22})$$

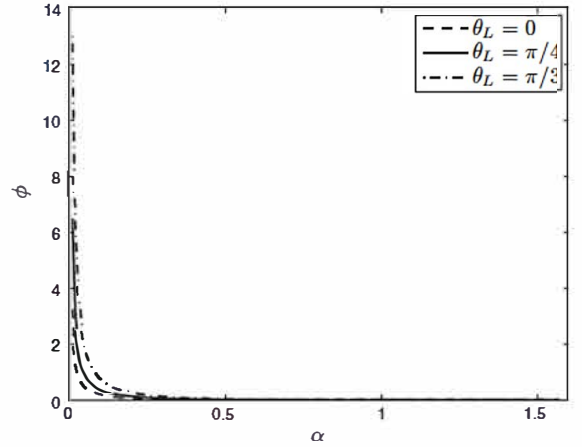
Now, since

$$2Y_*Y_0 = Y_*^2 - X_*^2 + 2X_*X_0, \quad (\text{C.23})$$

from (C.8) we have

$$2Y_* (af - ce) = (Y_*^2 - X_*^2) (ad - bc) + 2X_* (de - bf), \quad (\text{C.24})$$

Fig. 11 ϕ vs. α for
 $\theta_L = 0, \pi/4, \pi/3$
 $(\beta = \pi/3)$



and we need to consider whether

$$\phi := 2Y_*(af - ce) - (Y_*^2 - X_*^2)(ad - bc) - 2X_*(de - bf) \quad (\text{C.25})$$

is ever zero or not. Here, the idea is that we solve (5.10), subject to (5.12), (5.16) and

$$H_X(0) = -\tan(\pi/2 - \alpha), \quad (\text{C.26})$$

$$H_X(X_*) = -\tan \beta, \quad (\text{C.27})$$

where α and β are the angles that the curve $Y = H(X)$ makes with the Y - and X -axes, respectively; note that this computation is independent of θ_L , and that we merely sweep over all values of α and β , where $0 < \alpha, \beta < \pi/2$. Each computation generates values for X_* and Y_* , which are then used in (C.25). If it is found that ϕ is never zero, then this is an indication that X_0 and Y_0 cannot be found, and hence the sought-after circle does not exist. Numerical experimentation suggests that this indeed is the case. As an example, Fig. 11 shows ϕ vs. α for $\theta_L = 0, \pi/4, \pi/2$, for $\beta = \pi/3$, indicating that ϕ is never zero, no matter what value of θ_L is tried. Similar graphs were also obtained for other values of β .

Appendix D: $\theta_L = 0, \varepsilon = 0$

When $\varepsilon = 0$, we have $F \equiv 0$, and Eqs. (5.23)–(5.31) reduce to just

$$\frac{H_{XX}}{(1 + H_X^2)^{3/2}} = H + C_1, \quad (\text{D.1})$$

subject to

$$H_X(0) = -\cot \theta_L, \quad (\text{D.2})$$

$$H(X_*) = 0, \quad (\text{D.3})$$

$$H_X(X_*) = -\tan \theta_L, \quad (\text{D.4})$$

$$\int_0^{X_*} H(X) dX = \mathcal{A}. \quad (\text{D.5})$$

Multiplying (D.1) by H_X , integrating with respect to X and applying (D.3) and (D.4)

$$-\frac{1}{1 + H_X^2} = \frac{1}{2}H^2 + C_1H - \cos \theta_L. \quad (\text{D.6})$$

Alternatively, integrating (D.1) with respect to X and applying (D.2), (D.4) and (D.5) gives

$$\cos \theta_L - \sin \theta_L = \mathcal{A} + C_1 X_* \quad (\text{D.7})$$

Now, consider the behaviour of H near $X = X_*$ when $\theta_L = 0$. Since $H, H_X \ll 1$, we have, from (D.6),

$$\frac{H_X^2}{2} \sim \frac{H^2}{2} + C_1 H. \quad (\text{D.8})$$

If $C_1 \neq 0$, we have just

$$\frac{H_X^2}{2} \sim C_1 H, \quad (\text{D.9})$$

which leads to

$$H \sim \frac{1}{2}C_1 (X_* - X)^2. \quad (\text{D.10})$$

However, note that if $C_1 < 0$, which is clearly possible from (D.7) if $\mathcal{A} > 1$, then $H < 0$, which would be physically unrealistic. On the other hand, if $C_1 = 0$, i.e. $\mathcal{A} = 1$, we have, instead of (D.9),

$$H_X^2 \sim H^2, \quad (\text{D.11})$$

which would give $H \sim e^{\pm X}$. It is clear that only the behaviour with the minus sign is of relevance here. Taking this one, we see that an alternative to (D.10) is the possibility that the contact line extends to infinity with $H \sim e^{-X}$ as $X \rightarrow \infty$. In fact, for this case, there is an analytical solution for the meniscus given by [30–32]

$$X = \sqrt{2} - \ln \left(1 + \sqrt{2} \right) - \sqrt{4 - H^2} + \ln \left(\frac{2 + \sqrt{4 - H^2}}{H} \right). \quad (\text{D.12})$$

Finally, it is worth noting that, from the data in Table 1 and the values for h_0 and w_0 used in this paper, $\mathcal{A} \approx 0.02$, indicating that the relevant behaviour is that given by Eq. (D.10).

References

1. Terrill JR (1966) Diffusion of silicon in aluminum brazing sheet. *Weld Res Suppl* 45:202–209
2. Woods RA, Robinson IB (1974) Flow of aluminum dip brazing filler metals. *Weld Res Suppl* 53:S440–S445
3. Zhao H, Salazar AJ, Sekulic DP (2009) Analysis of fin-tube joints in a compact heat exchanger. *Heat Transf Eng* 30:931–940
4. Sekulic DP, Gao F, Zhao H, Zellmer B, Qian YY (2004) Prediction of the fillet mass and topology of aluminum brazed joints. *Weld J* 83:102S–110S
5. Sekulic DP (2001) Molten aluminum equilibrium membrane formed during controlled atmosphere brazing. *Int J Eng Sci* 39:229–241
6. Zellmer BP, Nigro N, Sekulic DP (2001) Numerical modelling and experimental verification of the formation of 2D and 3D brazed joints. *Model Simul Mater Sci Eng* 9:339–355
7. Sekulic DP, Zellmer BP, Nigro N (2001) Influence of joint topology on the formation of brazed joints. *Model Simul Mater Sci Eng* 9:357–369

8. Sekulic DP (2013) Modeling of the sequence of phenomena in brazing. In: Sekulic DP (ed) *Advances in brazing: science, technology and applications*. Woodhead Publishing, Cambridge, pp 55–81
9. Warren JA, Boettinger WJ, Roosen AR (1998) Modeling reactive wetting. *Acta Mater* 46(9):3247–3264
10. Su S, Yin L, Sun Y, Murray BT, Singler TJ (2009) Modeling dissolution and spreading of Bi-Sn alloy drops on a Bi substrate. *Acta Mater* 57(10):3110–3122
11. Villanueva W, Gronhagen K, Amberg G, Ågren J (2008) Multicomponent and multiphase modeling and simulation of reactive wetting. *Phys Rev E* 77, Article no. 056313
12. Villanueva W, Boettinger WJ, Warren JA, Amberg G (2009) Effect of phase change and solute diffusion on spreading on a dissolving substrate. *Acta Mater* 57:6022–6036
13. Villanueva W, Boettinger WJ, McFadden GB, Warren JA (2012) A diffuse-interface model of reactive wetting with intermetallic formation. *Acta Mater* 60:3799–3814
14. Braun RJ, Murray BT, Boettinger WJ, McFadden GB (1995) Lubrication theory for reactive spreading of a thin drop. *Phys Fluids* 7:1797–1810
15. Racz LM, Szekely J, Brakke KA (1993) A general statement of the problem and description of a proposed method of calculation for some meniscus problems in materials processing. *ISIJ Int* 33:328–335
16. Lacaze J, Jacques B, Mazet T, Vynnycky M (2018) Numerical simulation of brazing aluminium alloys with Al-Si alloys. *Trans Ind Inst Met* 71:2623–2629
17. Leal LG (2007) *Advanced transport phenomena: fluid mechanics and convective transport processes*. Cambridge series in Chemical Engineering, 1st edn. Cambridge University Press, Cambridge
18. Singler TJ, Su S, Yin L, Murray BT (2012) Modeling and experiments in dissolutive wetting: a review. *J Mater Sci* 47:8261–8274
19. Saiz E, Cannon RM, Tomsia AP (2000) Reactive spreading: adsorption, ridging and compound formation. *Acta Mater* 48:4449–4462
20. Saiz E, Tomsia AP, Cannon RM (1998) Ridging effects on wetting and spreading of liquids on solids. *Acta Mater* 46:2349–2361
21. Poirier DR (2014) Density, viscosity, and diffusion coefficients in hypoeutectic Al-Si liquid alloys: an assessment of available data. *Metall Mater Trans B* 45:1345–1354
22. Kobatake H, Brillo J, Schmitz J, Pichon P-Y (2015) Surface tension of binary Al-Si liquid alloys. *J Mater Sci* 50:3351–3360
23. Thermo-Calc Software TCAL version 2
24. Gao F, Sekulic DP, Qian YY, Ma X (2003) Residual clad formation and aluminum brazed joint topology prediction. *Mater Lett* 57:4592–4596
25. Huh C, Scriven LE (1971) Hydrodynamic model of steady movement of a solid/liquid/fluid contact line. *J Colloid Interface Sci* 35:85–101
26. Seppecher P (1996) Moving contact lines in the Cahn-Hilliard theory. *Int J Eng Sci* 34:977–992
27. Ehrhard P, Davis SH (1991) Nonisothermal spreading of liquid-drops on horizontal plates. *J Fluid Mech* 229:365–388
28. Su S (2012) The development of computational models for studying wetting, evaporation and thermal transport for electronics packaging applications. Ph.D. thesis, SUNY, Binghamton
29. Yang J, Yuan Q, Zhao YP (2018) Evolution of the interfacial shape in dissolutive wetting: coupling of wetting and dissolution. *Int J Heat Mass Transf* 118:201–207
30. Bikerman JJ (1970) *Physical surfaces*. Academic Press, New York
31. Vynnycky M, Zambrano M, Cuminato JA (2015) On the avoidance of ripple marks on cast metal surfaces. *Int J Heat Mass Transf* 58:43–54
32. Vynnycky M, Zambrano M (2018) Towards a “moving-point” formulation for the modelling of oscillation-mark formation in the continuous casting of steel. *Appl Math Mod* 63:243–265